

See discussions, stats, and author profiles for this publication at: <https://www.researchgate.net/publication/365662691>

Development of a semi-empirical interatomic potential appropriate for the radiation defects in V-Ti-Ta-Nb high-entropy alloy

Article in *Journal of Physics: Condensed Matter* · December 2022

DOI: 10.1088/1361-648X/aca50c

CITATIONS

2

9 authors, including:



Rongyang Qiu

Hunan University

9 PUBLICATIONS 44 CITATIONS

SEE PROFILE



Xichuan Liao

Hunan University

8 PUBLICATIONS 61 CITATIONS

SEE PROFILE

READS

97



Yangchun Chen

Hunan University

31 PUBLICATIONS 337 CITATIONS

SEE PROFILE



Yankun Dou

China Institute of Atomic Energy

16 PUBLICATIONS 192 CITATIONS

SEE PROFILE

PAPER

Development of a semi-empirical interatomic potential appropriate for the radiation defects in V-Ti-Ta-Nb high-entropy alloy

To cite this article: Rongyang Qiu *et al* 2023 *J. Phys.: Condens. Matter* **35** 055701

View the [article online](#) for updates and enhancements.

You may also like

- [Effect of final cooling temperature on the microstructure and mechanical properties of high-strength anti-seismic rebar](#)
Zeyun Zeng, Changrong Li, Zhiying Li et al.
- [Nanostructured Ti-Ta thin films synthesized by combinatorial glancing angle sputter deposition](#)
Yahya Motemani, Chinmay Khare, Alan Savan et al.
- [Retention of hydrogen in W-Ti-C, W-Ta-C and W-Zr-C alloys: *ab initio* study](#)
Yu-Wei You, Jiangying Yu, Hui Yuan et al.

Development of a semi-empirical interatomic potential appropriate for the radiation defects in V-Ti-Ta-Nb high-entropy alloy

Rongyang Qiu¹, Yangchun Chen¹, Xichuan Liao² , Yeping Lin^{1,*}, Yankun Dou³, Xinfu He³, Wen Yang³, Wangyu Hu² and Huiqiu Deng^{1,*} 

¹ School of Physics and Electronics, Hunan University, Changsha 410082, People's Republic of China

² College of Materials Science and Engineering, Hunan University, Changsha 410082, People's Republic of China

³ China Institute of Atomic Energy, Beijing 102413, People's Republic of China

E-mail: linyeping@hnu.edu.cn and hqdeng@hnu.edu.cn

Received 23 September 2022, revised 3 November 2022

Accepted for publication 22 November 2022

Published 14 December 2022



Abstract

High-entropy alloys (HEAs) hold promise as candidate structural materials in future nuclear energy systems. Body-centred cubic V-Ti-Ta-Nb HEAs have received extensive attention due to their excellent mechanical properties. In this work, the Finnis-Sinclair interatomic potential for quaternary V-Ti-Ta-Nb HEAs has been fitted based on the defect properties obtained with the density functional theory (DFT) calculations. The new potential for Nb accurately reproduces the vacancy formation energy, vacancy migration energy and interstitial formation energy. The typical radiation defect properties predicted by the alloy potential were consistent with the DFT results, including the binding energies between substitutional solute atoms, the binding energy between substitutional atoms and vacancies, and the formation energy of interstitial solute atoms. In addition, the mixing enthalpies of the alloys were also consistent with the DFT results. The present potential can also describe reasonably the collision cascade process of quaternary V-Ti-Ta-Nb HEAs.

Supplementary material for this article is available [online](#)

Keywords: Interatomic potential, defect properties, V-Ti-Ta-Nb alloys, High-entropy alloys

(Some figures may appear in colour only in the online journal)

1. Introduction

High-entropy alloys (HEAs) represent a novel alloy design strategy developed in recent years [1–9], which are usually composed of four or more elements at or near equi-atomic ratios. Due to the high configurational entropy, these

compositionally complex alloys tend to form a single-phase solid solution structure with a single crystal lattice, such as body-centered cubic (BCC) [10, 11], face-centered cubic (FCC) [12, 13] or hexagonal close-packed (HCP) lattice [13–15]. And HEAs have been considered as promising candidate structural materials for future fusion and fission reactors [6, 16] because of their excellent properties, e.g. excellent mechanical properties [17–20], high oxidation resistance [21], high corrosion resistance [22] and radiation resistance [19, 23–26].

* Authors to whom any correspondence should be addressed.

The most studied HEAs in recent years are those based on 3d transition metals Al, Co, Cr, Cu, Fe, Mn, Ni, Ti, and V [2, 27–30], which exhibit excellent strength, high ductility, and good toughness at low temperatures [12, 13, 27–30]. Refractory HEAs are composed of refractory elements with high melting points (Cr, Hf, Mo, Nb, Ta, Ti, V, W, and Zr), which maintain high strength at temperatures up to 1600 °C [31], were first reported in 2010 by Senkov *et al* [10]. Subsequent studies have shown that refractory HEAs have excellent radiation resistance with little radiation hardening and no radiation-induced dislocation loops even at high radiation doses [32–35]. Refractory HEAs have attracted considerable attention of researchers due to their excellent radiation resistance and good high-temperature mechanical properties.

V-Ti-Ta-Nb alloys have been widely reported in recent years as refractory HEAs [36–38]. Yao *et al* [39] showed that V-Ti-Ta-Nb HEA is very ductile and does not fracture up to 50% strain. Lee *et al* [37] studied the yield strength of the NbTaTiV, MoNbTaW and MoNbTaVW refractory HEAs, as well as conventional alloys, titanium-based alloys and nickel-based superalloys at elevated temperatures. The yield strength of other alloys decreases sharply at certain temperatures compared to refractory HEA. However, refractory HEA, NbTaTiV, MoNbTaW and MoNbTaVW, do not show a significant decrease in yield strength with temperature. Furthermore, the yield strength of the NbTaTiV and MoNbTaVW HEAs is much higher than the other alloys at temperatures over 800 °C. In addition, some V-Ti-Ta-Nb-based HEAs also show excellent mechanical properties, e.g. the V-Ti-Ta-Nb-Mo HEA has a compressive strain of approximately 30% before fracture and has a large work-hardening capacity [38]. Although the V-Ti-Ta-Nb refractory HEA has excellent mechanical properties, the practical application of this material usually faces many challenges. One of the biggest problems facing materials as structural candidates for future fusion reactors is exposure to large numbers of particles. A large number of radiation defects will be produced, thereby reducing the performance of the material and affecting the service life of the reactor. The study of radiation damage of V-Ti-Ta-Nb HEA is crucial for evaluating the properties of V-Ti-Ta-Nb materials. Because of the difficulty of irradiation experiments in nuclear reactors, computational simulation methods are increasingly used as a means to understand the properties of irradiated materials. Among numerous simulation methods, large-scale molecular dynamics (MD) and Monte Carlo (MC) simulations have been widely used. However, MD and MC simulations require potentials to accurately describe the interactions between atoms, and there is no report on the interatomic potential of V-Ti-Ta-Nb quaternary alloys up to now.

In this work, we develop a semi-empirical Finnis-Sinclair (FS) potential for V-Ti-Ta-Nb quaternary alloys based on our recently developed V-Ti-Ta ternary potential [40]. There are some empirical potentials for pure element Nb, e.g. the embedded atom method (EAM) potential of Feller *et al* (EAM-1) [41] and Cheng *et al* (EAM-2) [42], and the modified embedded atom method (MEAM) potential of Yang and Qi [43]. The lattice parameters, elastic constants, bulk modulus and

surface energy of BCC Nb crystal obtained by these potentials are close to the experimental or first principles density functional theory (DFT) calculations values [41, 44–47]; however, these potentials are still lacking in the description of some typical point defects (such as interstitial formation energy, vacancy formation energy and migration energy) produced by irradiation, especially the predictions of the most stable interstitial formation energies that are inconsistent with the DFT results [41, 48]. The DFT calculation results show that the most stable interstitial in Nb bulk is <111> dumbbell, while the most stable interstitial structures predicted by EAM-1 [41], EAM-2 [42] and MEAM [43] potentials are <110> dumbbell, <111> crowdion and <100> dumbbell, respectively. An accurate description of the most stable interstitial defects is crucial for modelling radiation damage and defect evolution. To be consistent with the FS form of our V, Ti and Ta element potentials and accurately describe the point defect properties of the Nb element, we consider refitting the Nb potential. To achieve the full potential parameterization for the V-Ti-Ta-Nb quaternary system, new Nb-Nb, V-Nb, Ta-Nb and Ti-Nb interatomic potentials are fitted in this study based on the FS formalism.

2. Modelling and methods

Based on our recently developed FS potential of the V-Ti-Ta ternary system [40], a full potential parameterization of the V-Ti-Ta-Nb system is fitted. Ten sets of potential parameters are required for the V-Ti-Ta-Nb system: six sets for the interactions of V-V, Ti-Ti, Ta-Ta, V-Ti, V-Ta and Ta-Ti interactions, four sets for the interactions of Nb-Nb, V-Nb, Ti-Nb and Ta-Nb. The first six groups of interatomic potentials were taken from Chen *et al* [49, 50] and Qiu *et al* [40], while the last four groups of interatomic potentials were fitted here. The specific form of the potential can refer to our previous work [40, 49–52], and some main formulas are given here. The total potential energy E of the system is expressed as

$$E = \frac{1}{2} \sum_{ij} V(r_{ij}) + \sum_i F(\rho_i) \quad (1)$$

where $V(r_{ij})$ is a pair potential term as a function of the distance r_{ij} between i atom and j atom. The many-body term $F(\rho_i)$ as a function of the local electron density ρ_i is written as

$$F(\rho_i) = -A\sqrt{\rho_i}, \quad (2)$$

where the parameter A in equation (2) is set to (1). The local electron density ρ_i is a linear superposition of the charge densities φ of surrounding atoms at the i atom:

$$\rho_i = \sum_j \varphi(r_{ij}) \quad (3)$$

The pair potential function $V(r)$ and density function $\varphi(r)$ for pure elements are defined as

$$V(r) = \sum_{k=1}^{n_k} d_k (r_k - r)^3 H_s(r_k - r), \quad (4)$$

$$\varphi(r) = \sum_{k=1}^{n_k} D_k (R_k - r)^3 H_s(R_k - r) . \quad (5)$$

Here, $H_s(x)$ is the Heaviside step function, d_k and D_k are the knot coefficients, and r_k and R_k are the positions of cubic spline knots.

The pure elemental potentials have been determined using invariant transformations [53, 54] before fitting the cross-potential functions. The pair potential function $V(r)$ for the cross potential is defined by the linear combination of the pure element pair potential functions:

$$V_{AB}(r) = \frac{1}{2} \left[U_A V_{AA} \left(r \frac{r_A}{r_C} \right) + U_B V_{BB} \left(r \frac{r_B}{r_C} \right) \right], \quad (6)$$

$$r_C = \frac{1}{2} [r_1(A) + r_1(B)] . \quad (7)$$

Here, r_A, r_B, U_A and U_B are the fitted parameters, $r_1(A)$ and $r_1(B)$ are the first neighbour distance of element A and element B. The cross-density function φ_{AB} is defined as follows:

$$\varphi_{AB}(r) = \sum_{k=1}^{n_k} T_k (R_k - r)^3 H_s(R_k - r), \quad (8)$$

where the T_k is the knots coefficient.

To better describe the collision cascade process, the short-range part ($r < r_m$) of the pair potential is described by the Ziegler-Biersack-Littmark (ZBL) function [55]. Then the short-range ZBL function part and the near-equilibrium part ($r > r_n$) are smoothly connected by the connection function ($r_m < r < r_n$). The connection function expression is defined as follows:

$$V_{\text{connect}}(r) = e^{(c_1 + c_2 r + c_3 r^2 + c_4 r^3)}, \quad (9)$$

where the c_i coefficient is determined by the continuity of the potential function and its first derivative.

The simulated annealing method [56] and conjugate gradient algorithm [57] were used for the fitting process. And the final potential parameters are derived by minimizing the weighted mean square deviation of the computed property from its target value. For pure element Nb, the fitted target properties include lattice constant, cohesive energy, elastic constant, bulk modulus, structural energy difference, vacancy formation energy, interstitial formation energy (including $\langle 111 \rangle$, $\langle 110 \rangle$ and $\langle 100 \rangle$ dumbbell, tetrahedron and octahedron) and the equation of state for BCC lattice (Rose's equation [58]). For the alloy- (or cross-) potentials, some typical radiation defects of the V-based alloy systems were considered, including the formation energy of a solute-substituted atom, the binding energy of the solute-substituted atoms, and the binding energy of the solute-substituted atoms and a vacancy. Detailed definitions of the corresponding formation and binding energies can be found in our previous study [52] and will not be given here. The energies of various defects were obtained using a dynamic fitting method [59]. The corresponding defect configurations were obtained by deleting and adding corresponding atoms in a $10a \times 10a \times 10a$ box during the fitting process (a is the lattice parameter of alloy).

In this work, as did in most of the empirical potential fitting work [50, 60, 61], the target values of lattice constant, cohesive energy, bulk mode and elastic constants are from experimental results, and the target values of defects formation and binding energies are from DFT calculations. However, as far as we know, no complete defect properties of the alloy systems described above can be found in previous literature. Therefore, we calculated many of the corresponding defects using the DFT method in the present manuscript. The Vienna *ab-initio* Simulation Package [62, 63] with the Projector Augmented Wave method [64] was used to perform the DFT calculations. The Fermi level smearing width was set to 0.2 eV and the plane wave cutoff was set to a higher value of 500 eV. All results in this paper were obtained using a BCC supercell with 128 atoms ($4a \times 4a \times 4a$), and the Brillouin zone was sampled with $3 \times 3 \times 3$ k points using the Monkhorst-Pack scheme. Furthermore, the position of the atoms and the volume of the cell were completely relaxed until the force on each atom was less than $0.01 \text{ eV } \text{\AA}^{-1}$.

Table 1 lists the potential parameters of pure Nb and the cross-terms Nb-V, Nb-Ti and Nb-Ta, as well as the parameters of the ZBL function [55] and invariant transformation (s and c). Figure 1 shows that the curves of the fitted potential functions are smooth in all regions.

3. Results and discussion

3.1. Validation of the fitted Nb potential

Table 2 lists the properties of Nb predicted by the present potential and compared them with the results of DFT [41, 43] (including DFT results calculated by this work), experiments [44–47] and other empirical potentials [41–43]. Properties considered include lattice constant, cohesive energy, bulk modulus, elastic constants (C_{11} , C_{12} and C_{44}), structural energy difference, vacancy formation energy, vacancy migration energy, vacancy diffusion activation energy, interstitial formation energy ($E_i^f \langle 111 \rangle$ d, $E_i^f \langle 111 \rangle$ c, $E_i^f \langle 110 \rangle$ d, $E_i^f \langle 100 \rangle$ d, E_{Tet}^f and E_{Oct}^f), surface energy (E_{100}^{surf} , E_{110}^{surf} , E_{111}^{surf} and E_{112}^{surf}), stacking fault energy (E_{110}^{SF} and E_{112}^{SF}) and melting point. In addition, we have calculated the properties of some typical defects in Nb using DFT and are close to the results of other DFT calculations [41, 43]. The properties indicated by “*” are included in the potential fitting process. For the lattice constants, the results of the four potentials are close to the results of DFT (3.309 Å [41] and 3.308 Å calculated by this work) and the experimental (3.303 Å [44]). The cohesive energy predicted by the present potential is the same as the experimental value (7.57 eV) [45]. The calculated bulk modulus and elastic constants of the four potentials are close to the DFT and experimental values, except that the EAM-2 potential underestimates the value of C_{11} and the MEAM potential underestimates the value of C_{44} . The energies of FCC, HCP, diamond, A15 and simple cubic (SC) structure predicted by the present potential are higher than that of the BCC lattice, which proves that the BCC lattice is the ground state structure.

Table 1. Potential parameters for the V-Ti-Ta-Nb systems fitted in this work, including Nb, Nb-Ti, Nb-V and Nb-Ta. Parameters for the invariant transformation and ZBL connection function are also listed in the table. The units of energy and distance are eV and Å, respectively. The potential parameters of the Ta, V, Ti, V-Ti, V-Ta and Ta-Ti can be found in [40, 49, 50].

| Nb | | | |
|------------------------------------|---|------------------------------------|---|
| D ₁ (R ₁) | $0.228970461208629 \times 10^{+0}$ (5.6) | d ₁ (r ₁) | $0.406232771298125 \times 10^{-2}$ (5.6) |
| D ₂ (R ₂) | $-0.143773704606611 \times 10^{+0}$ (5.1) | d ₂ (r ₂) | $-0.392280620498316 \times 10^{-1}$ (5.2) |
| D ₃ (R ₃) | $0.442520279596159 \times 10^{+0}$ (4.7) | d ₃ (r ₃) | $0.997330286805649 \times 10^{-2}$ (4.9) |
| D ₄ (R ₄) | $-0.119238586627089 \times 10^{+1}$ (4.3) | d ₄ (r ₄) | $0.672012127675162 \times 10^{-2}$ (4.6) |
| D ₅ (R ₅) | $0.533932879173870 \times 10^{+1}$ (3.9) | d ₅ (r ₅) | $-0.814822043534348 \times 10^{-1}$ (4.4) |
| D ₆ (R ₆) | $0.267296333522721 \times 10^{+0}$ (3.5) | d ₆ (r ₆) | $-0.108289958467816 \times 10^{-1}$ (4.2) |
| D ₇ (R ₇) | $-0.853585331047410 \times 10^{+0}$ (3.1) | d ₇ (r ₇) | $0.386463726152318 \times 10^{+0}$ (4.0) |
| D ₈ (R ₈) | $0.152679909461795 \times 10^{+2}$ (2.8) | d ₈ (r ₈) | $0.295747347897325 \times 10^{+0}$ (3.8) |
| D ₉ (R ₉) | $-0.355429026208721 \times 10^{+2}$ (2.6) | d ₉ (r ₉) | $0.752118138478126 \times 10^{+0}$ (3.6) |
| D ₁₀ (R ₁₀) | $0.441202948805206 \times 10^{+3}$ (2.4) | d ₁₀ (r ₁₀) | $0.810873167989606 \times 10^{+0}$ (3.4) |
| r _m | $+0.100000000000000 \times 10^{+1}$ | d ₁₁ (r ₁₁) | $-0.291234124764112 \times 10^{+1}$ (3.2) |
| r _n | $+0.200000000000000 \times 10^{+2}$ | d ₁₂ (r ₁₂) | $0.185529113174097 \times 10^{+2}$ (3.0) |
| c ₁ | $0.973561270770035 \times 10^{+1}$ | d ₁₃ (r ₁₃) | $0.212475894823030 \times 10^{+2}$ (2.8) |
| c ₂ | $-0.438410474315553 \times 10^{+1}$ | d ₁₄ (r ₁₄) | $-0.429287143700332 \times 10^{+2}$ (2.7) |
| c ₃ | $0.265687659281890 \times 10^{-1}$ | d ₁₅ (r ₁₅) | $0.193808797170267d \times 10^{+2}$ (2.6) |
| c ₄ | $-0.292989690799231 \times 10^{-1}$ | d ₁₆ (r ₁₆) | $-0.660586542241854 \times 10^{+0}$ (2.5) |
| s | $0.113652266685082 \times 10^{-1}$ | d ₁₇ (r ₁₇) | $0.633867939383165d \times 10^{+2}$ (2.4) |
| c | $0.533039085539423 \times 10^{-1}$ | | |

| Nb-Ti | | Nb-V | | Nb-Ta | |
|----------------------------------|---|------|---|-------|--|
| T ₁ (R ₁) | $0.139853938297063 \times 10^{-1}$ (4.9) | | $0.108049066074715 \times 10^{-1}$ (4.9) | | $0.004822211146355 \times 10^{+0}$ (4.9) |
| T ₂ (R ₂) | $-0.301723719223554 \times 10^{-1}$ (4.0) | | $-0.178113625179064 \times 10^{-1}$ (4.0) | | $0.021624536449734 \times 10^{+0}$ (4.0) |
| T ₃ (R ₃) | $0.168338660568803 \times 10^{+0}$ (3.1) | | $0.516762583323153d \times 10^{+0}$ (3.1) | | $0.100357447847642 \times 10^{+0}$ (3.1) |
| T ₄ (R ₄) | $0.828566551208496 \times 10^{+1}$ (2.5) | | $-0.398486891710423 \times 10^{+0}$ (2.5) | | $4.158796646129530 \times 10^{+0}$ (2.5) |
| U _A | $0.185307303907643 \times 10^{+0}$ | | $0.175448666464753 \times 10^{+1}$ | | $0.721833935668948 \times 10^{+0}$ |
| U _B | $0.204009893850390 \times 10^{+1}$ | | $0.408293152515588 \times 10^{+1}$ | | $1.155726936867270 \times 10^{+0}$ |
| r _A | $0.269340612786304 \times 10^{+1}$ | | $0.277476923258605 \times 10^{+1}$ | | $2.920603790480810 \times 10^{+0}$ |
| r _B | $0.268520832221073 \times 10^{+1}$ | | $0.416138332658539 \times 10^{+1}$ | | $2.686078293143230 \times 10^{+0}$ |
| r _C | $2.846727250000000 \times 10^{+0}$ | | $2.740970401200000 \times 10^{+0}$ | | $2.728078486730000 \times 10^{+0}$ |
| r _m | $+0.100000000000000 \times 10^{+1}$ | | $+0.100000000000000 \times 10^{+1}$ | | $+0.100000000000000 \times 10^{+1}$ |
| r _n | $+0.200000000000000 \times 10^{+1}$ | | $+0.200000000000000 \times 10^{+1}$ | | $+0.200000000000000 \times 10^{+1}$ |
| c ₁ | $0.896245536949933 \times 10^{+1}$ | | $0.803737550421045 \times 10^{+1}$ | | $0.106433437844975 \times 10^{+2}$ |
| c ₂ | $-0.401286466420163 \times 10^{+1}$ | | $-0.294624421530725 \times 10^{+1}$ | | $-0.494111273134629 \times 10^{+1}$ |
| c ₃ | $0.555711100787719 \times 10^{-1}$ | | $0.283779458282806d \times 10^{+0}$ | | $-0.111015855800290 \times 10^{+0}$ |
| c ₄ | $-0.627842509913231 \times 10^{-1}$ | | $-0.402677515673619d \times 10^{+0}$ | | $0.110318335820441 \times 10^{+0}$ |

The vacancy migration energy affects the migration of vacancy defects (the higher the vacancy migration energy, the less likely they are to migrate) and thus the microscopic evolution of vacancy defects. Therefore, the ability of the interatomic potential to reasonably predict vacancy migration energy is crucial for the microscopic evolution of vacancy defects. The vacancy formation energies predicted by the EAM-2 [42] (2.83 eV) and the present potential (2.72 eV) are close to the calculated values of DFT (2.72 eV [41], 2.77 eV [65] and 2.71 eV calculated by this work), while the predicted values by the EAM-1 [41] (3.10 eV) and MEAM [43] (2.10 eV) potentials have some deviations (about 14% and 23%, respectively) from the DFT calculation result. The vacancy migration energy predicted by the present potential is 0.46 eV, which is close to the DFT results (0.55 eV [41], 0.43 eV [65] and 0.53 eV calculated by this work). The

EAM-1 [41] (0.77 eV) and MEAM [43] (0.92 eV) potentials overestimate the vacancy migration energy and the deviations from the DFT results are about 54% and 84%, respectively. In addition, compared with the EAM-1 [41] and MEAM [43] potentials, the vacancy diffusion activation energy predicted by the present potential is closer to the calculated value of DFT [41]. Different from vacancy defects, the interstitial defects have many configurations (including <100> dumbbell, <110> dumbbell, <111> dumbbell, <111> crowdion, tetrahedral and octahedral interstitial), which will affect the types of defect clusters (such as dislocation loop), and then affect the microscopic evolution of defects. The most stable interstitial defect predicted by the present potential is the <111> dumbbell (4.13 eV), which is consistent with the DFT results and close to the DFT values (3.95 eV [41], 4.34 eV [48] and 3.92 eV calculated by this work). However, the most

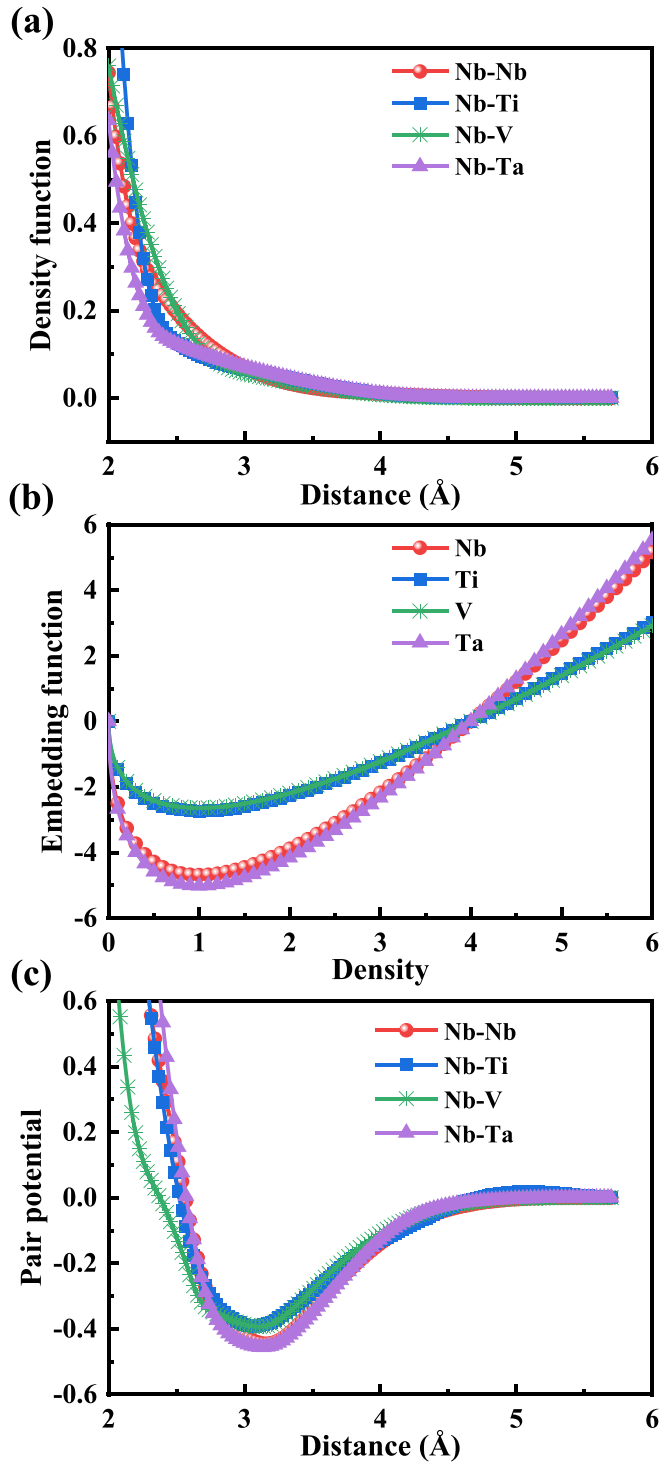


Figure 1. Dependence of the potential functions on atomic distance or electronic density: (a) density functions, (b) embedding functions and (c) pair potentials.

stable interstitial structures predicted by EAM-1 [41], EAM-2 [42] and MEAM [43] are $\langle 110 \rangle$ dumbbell, $\langle 111 \rangle$ crowdion and $\langle 100 \rangle$ dumbbell, respectively. Figure 2 shows the overall trend of present potential predicting interstitial defects and compared with results obtained with DFT [41, 48] (including the results calculated by this work) and other empirical

potentials [41–43]. From the overall perspective of figure 2, compared with other potentials, the predicted results of the present Nb potential are closer to the DFT results. And the most stable interstitial predicted by the present potentials is consistent with the DFT calculation. Compared with other potentials, the present potential may be more suitable for radiation defects simulation.

For the surface energy, the predicted results by the present potential and EAM-1 potential [41] are close to the DFT value, the deviation is within 6%, while EAM-2 [42] overestimates the surface energy (30%–40%), and MEAM [43] underestimates the surface energy (2%–20%). The present potential, EAM-1 [41] and MEAM [43] potential predict stacking fault energy all in agreement with the DFT value [43], within 8% of the deviation. For the melting point, the present potential and EAM-1 [41] predicted values were 2650 ± 10 K and 2685 ± 5 K, respectively. The predicted value is close to the experimental value of 2750 K [44], and the deviation is within 4%.

In radiation damage, point defects can aggregate to form larger defect clusters, such as dislocation loops. The properties of dislocation loops will affect the micro-evolution of the material, which is very important to the properties of the material. Experimental observations show that there are $1/2\langle 111 \rangle$ and $\langle 100 \rangle$ dislocation loops in BCC transition metals irradiated at low temperatures [66–69], of which the main dislocation loops are $1/2\langle 111 \rangle$ dislocation loops. The relative stability of the $1/2\langle 111 \rangle$ and $\langle 100 \rangle$ interstitial dislocation loops in Nb at 0 K was predicted by the present potential. The simulation box of the $\langle 100 \rangle$ dislocation loop consists of $32a \times 32a \times 32a$ cell units along the [100], [010] and [001] directions and contains 65 536 atoms. The simulation box of the $1/2\langle 111 \rangle$ dislocation loop consists of $45x \times 12y \times 20z$ cell units ($x = \frac{\sqrt{3}}{2}a$, $y = \sqrt{6}a$ and $z = \sqrt{2}a$) along the [111], $[1\bar{1}\bar{2}]$ and $[\bar{1}10]$ directions and contains 64 800 atoms. Figure 3 shows the formation energy of $\langle 100 \rangle$ and $1/2\langle 111 \rangle$ interstitial dislocation loops as a function of the size of the dislocation loops in Nb, where the dislocation loops contain up to 300 atoms. As shown in figure 3, the formation energies of the $1/2\langle 111 \rangle$ and $\langle 100 \rangle$ loops gradually increase with the size of the dislocation loops. And the formation energy of $1/2\langle 111 \rangle$ dislocation loops containing the same number of atoms is lower than that of $\langle 100 \rangle$ loops. Compared with the $\langle 100 \rangle$ dislocation loop, the energy of the $1/2\langle 111 \rangle$ loop is favourable at all sizes, indicating that the most stable structure of the interstitial dislocation loop is the $1/2\langle 111 \rangle$ loop. That is consistent with the experimental results at low temperatures [66–69].

3.2. Validation of the fitted quaternary V-Ti-Ta-Nb potential

3.2.1. Point defect properties. Solute atoms and their interaction with irradiation defects will affect the microstructure and evolution of the materials. In this section, we calculated the defect properties of Nb, Ti and Ta as solute atoms in V and the defect properties of V, Ti and Ta as solute atoms in Nb by the present potential, and compared them with our DFT results.

Table 2. The physical properties of Nb are calculated using this potential and compared with experimental values and DFT or other empirical potential calculations. Including lattice parameter a (Å), cohesive energy E_c (eV), bulk modulus B (GPa), elastic constants C_{11} , C_{12} and C_{44} (GPa), structural energy difference ΔE (eV/atom), vacancy formation energy E_v^f (eV), vacancy migration energy E_v^m (eV), interstitial formation energy (eV), surface energy E_{100}^{surf} , E_{110}^{surf} , E_{111}^{surf} and E_{112}^{surf} (J m⁻²), stacking fault energy (mJ m⁻²) and melting point (K). The properties indicated by “*” are included in the potential fit.

| Property | DFT | Exp. | FS Present | EAM-1 [41] | EAM-2 [42] | MEAM [43] |
|------------------------|--|----------------------|------------|------------|------------|-----------|
| Lattice properties | | | | | | |
| a^* | 3.309 ^a 3.308 | 3.303 ^e | 3.30 | 3.308 | 3.297 | 3.322 |
| E_c^* | 7.10 ^a 7.07 | 7.57 ^f | 7.57 | 7.09 | 7.470 | 7.00 |
| B^* | 172 ^a | 173 ^g | 173 | 172 | 170 | 173 |
| C_{11}^* | 251 ^a | 253 ^g | 252 | 244 | 215 | 250 |
| C_{12}^* | 133 ^a | 133 ^g | 133 | 136 | 147 | 135 |
| C_{44}^* | 22 ^a | 31 ^g | 35 | 32 | 32 | 21 |
| a_{fcc} | 4.217 ^a | | 4.232 | 4.157 | 4.167 | 4.232 |
| $\Delta E_{fcc-bcc}^*$ | 0.324 ^a | | 0.119 | 0.187 | 0.189 | 0.321 |
| a_{hcp} | 2.867 ^a | | 2.992 | 2.940 | 2.880 | 2.850 |
| c_{hcp} | 5.238 ^a | | 7.456 | 4.800 | 5.040 | 5.339 |
| $\Delta E_{hcp-bcc}^*$ | 0.297 ^a | | 0.114 | 0.187 | 0.138 | 0.290 |
| a_{A15} | | | 6.157 | 5.915 | | 5.358 |
| $\Delta E_{A15-bcc}$ | | | 2.326 | 2.236 | | 0.226 |
| a_{sc} | | | 2.703 | 2.583 | | 2.678 |
| ΔE_{sc-bcc} | | | 0.812 | 1.06 | | 0.81 |
| Point defect | | | | | | |
| E_v^{f*} | 2.72 ^a 2.77 ^b 2.71 | 2.6–3.1 ^h | 2.72 | 3.10 | 2.83 | 2.10 |
| E_v^{m*} | 0.55 ^a 0.43 ^b 0.53 | 0.6–1.6 ^h | 0.46 | 0.77 | | 0.92 |
| Q_v | 3.27 ^a 3.20 ^b 3.24 | | 3.18 | 3.87 | | 3.02 |
| $E_i^f <111>d^*$ | 3.95 ^a 4.34 ^c 3.92 | | 4.13 | 4.09 | 4.78 | 4.18 |
| $E_i^f <111>c^*$ | 3.99 ^a 4.35 ^c 3.93 | | 4.14 | 4.02 | 4.56 | 4.18 |
| $E_i^f <110>d^*$ | 4.31 ^a 4.65 ^c 4.28 | | 4.46 | 3.83 | 4.76 | 4.43 |
| $E_i^f <100>d^*$ | 4.76 ^a 5.02 ^c 4.67 | | 4.67 | 4.50 | 4.76 | 4.02 |
| $E_i^f Tet^*$ | 4.56 ^a 4.90 ^c 4.55 | | 4.57 | 4.37 | 4.97 | 4.12 |
| $E_i^f Oct^*$ | 4.89 ^a 5.08 ^c 4.79 | | 4.65 | 4.36 | 4.76 | 4.41 |
| Surface energy | | | | | | |
| E_{100}^{surf} | 2.34 ^a | | 2.23 | 2.36 | 3.15 | 2.12 |
| E_{110}^{surf} | 2.10 ^a | | 1.97 | 2.04 | 2.95 | 1.64 |
| E_{111}^{surf} | 2.39 ^a | | 2.43 | 2.47 | 3.11 | 2.43 |
| Stacking fault | | | | | | |
| $E_{110}^{SF}(111)$ | 690.46 ^d | | 639.03 | 720 | | 727.31 |
| $E_{112}^{SF}(111)$ | 801.00 ^d | | 729.36 | 820 | | 879.50 |
| T_m | | 2750 ^e | 2650 ± 10 | 2685 ± 5 | | |

^a Fellinger *et al* [41].

^b Shang *et al* [65].

^c Cerdeira *et al* [48].

^d Yang and Qi [43].

^e Roberge [44].

^f Kittel [45].

^g Simmons and Wang [46].

^h Ullmaier [47].

Table 3 shows the properties of the solute atoms V, Ta and Ti as substitution defects in the BCC Nb bulk calculated by the present potential, and compared with our DFT results. The formation energy of one substitutional V in bulk Nb calculated by the present potential is 0.24 eV, which is slightly lower than the DFT value of 0.35 eV. The binding energies of the two substitutional V atoms at the first and second nearest neighbour sites are 0.02 eV and 0.02 eV, respectively, which are close to

the DFT results of 0.02 eV and 0.04 eV. The properties of the substitutional solutes Ta and Ti in the Nb bulk are also consistent with the DFT results. Positive binding energy indicates that the two substitutional atoms are attractive, and negative binding energy indicates two substitutional atoms are repulsive. The present potential shows that the two substitutional V atoms in Nb are attractive at the first and second neighbours; the two substitutional Ti atoms in Nb are attractive at the first

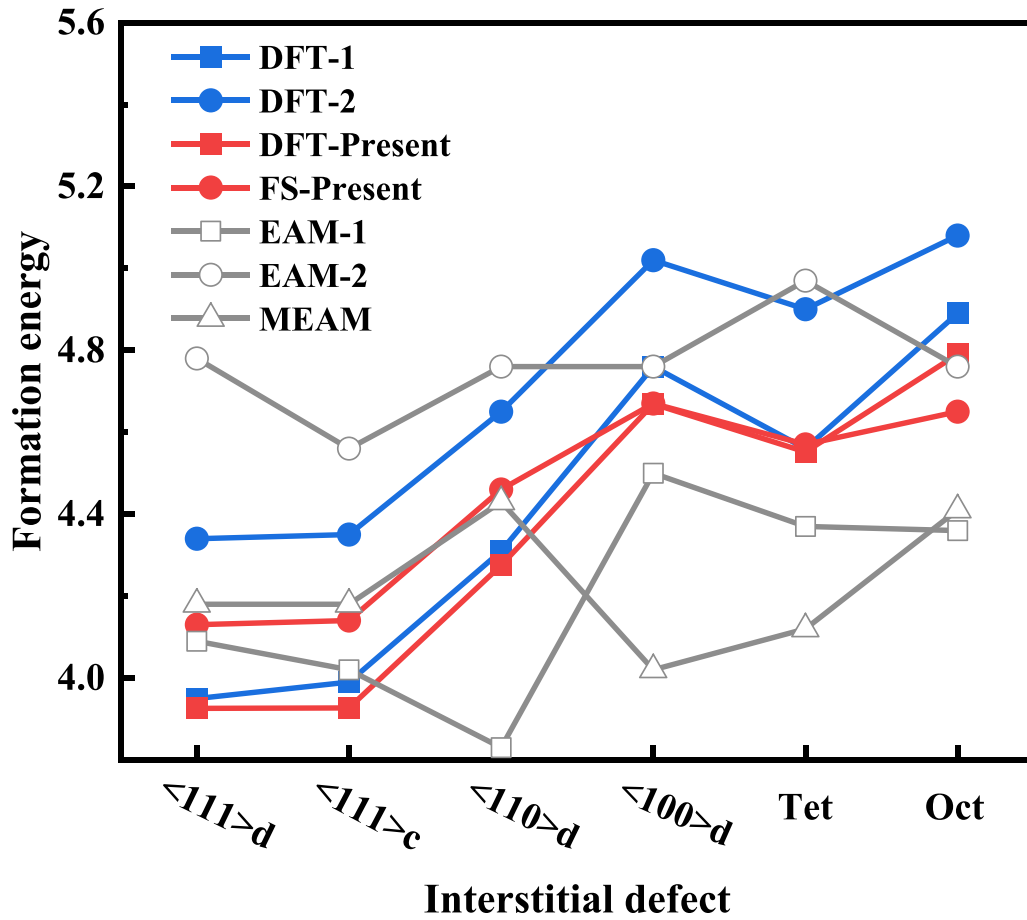


Figure 2. The self-interstitial defect properties of Nb are calculated by the present potential, including $\langle 100 \rangle$ dumbbell, $\langle 110 \rangle$ dumbbell, $\langle 111 \rangle$ dumbbell, $\langle 111 \rangle$ crowdon, tetrahedral and octahedral interstitial, and compared with DFT value (DFT-1 [41] and DFT-2 [48] and DFT-Present calculated by this work) and other embedded potential results (EAM-1 [41], EAM-2 [42] and MEAM [43]).

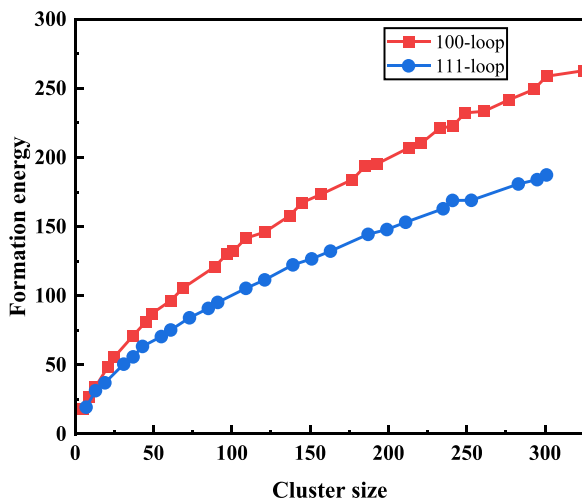


Figure 3. The current potential predicts the formation energy of $1/2\langle 111 \rangle$ dislocation loops and $\langle 100 \rangle$ dislocation loops of Nb as a function of loop size.

nearest neighbour and repulsive in the second nearest neighbour; the two substitutional Ta atoms in Nb are very weak at the first and second nearest neighbours. This is consistent with the DFT results.

Table 3. The properties of the solute atoms V, Ta and Ti as substitution defects in the BCC bulk Nb were calculated by the present potential and compared with the DFT results.

| Property | FS present | DFT |
|------------------------------|------------|-------|
| E_{sub}^f (V) | 0.24 | 0.35 |
| $E_{1\text{nn}}^b$ (V – V) | 0.02 | 0.02 |
| $E_{2\text{nn}}^b$ (V – V) | 0.02 | 0.04 |
| E_{sub}^f (Ti) | 0.13 | 0.19 |
| $E_{1\text{nn}}^b$ (Ti – Ti) | 0.02 | 0.02 |
| $E_{2\text{nn}}^b$ (Ti – Ti) | –0.05 | –0.06 |
| E_{sub}^f (Ta) | –0.02 | 0.02 |
| $E_{1\text{nn}}^b$ (Ta – Ta) | 0 | 0 |
| $E_{2\text{nn}}^b$ (Ta – Ta) | –0.01 | 0.00 |

Table 4 summarizes the defect properties of Nb as a solute atom in the V bulk predicted by the present potential and compared it with the DFT results. The formation energies of one substituted Nb atom in bulk V calculated by the present potential are 0.25 eV, which is equal to the DFT result. The binding energies of the two substituted Nb atoms at the first and second nearest neighbour sites are 0.02 eV and 0.04 eV, respectively, which are the same as the DFT results. The binding energies between a substituted Nb atom and a vacancy located at the

Table 4. Summary of the key properties of solute atom Nb as the point defects in BCC bulk V calculated by the present potential in comparison with our DFT calculations. Including the formation energy of a substitution atom, the formation energy of a mixed dumbbell and pure solute dumbbell, the binding energy of two substitution atoms, the binding energy of a substitution atom and a vacancy, the binding energy between a solute atom and self-interstitial atom, the binding energy of pure solute dumbbell.

| Property | FS present | DFT |
|----------------------------------|------------|----------|
| E_{sub}^f (Nb) | 0.25 | 0.25 |
| $E_{1\text{nn}}^b$ (Nb – Nb) | 0.02 | 0.02 |
| $E_{2\text{nn}}^b$ (Nb – Nb) | 0.04 | 0.04 |
| $E_{1\text{nn}}^b$ (Nb – Vac) | 0.25 | 0.38 |
| $E_{2\text{nn}}^b$ (Nb – Vac) | −0.04 | −0.04 |
| E_{111}^f (Nb – V) | 3.93 | 3.60 |
| $dE_{110-111}^f$ (Nb – V) | 0.24 | 0.40 |
| $dE_{100-111}^f$ (Nb – V) | Unstable | Unstable |
| $dE_{\text{Oct}-111}^f$ (Nb – V) | 0.60 | 0.87 |
| $dE_{\text{Tet}-111}^f$ (Nb – V) | 0.44 | 0.44 |
| E_{111}^b (Nb – V) | −0.31 | −0.49 |
| E_{111}^f (Nb – Nb) | 4.50 | 4.36 |
| $dE_{110-111}^f$ (Nb – Nb) | 0.41 | 0.51 |
| $dE_{100-111}^f$ (Nb – Nb) | 0.83 | 0.91 |
| E_{111}^b (Nb – Nb) | −0.32 | −0.51 |

first and second nearest neighbours sites are close to the DFT results. The present potential predicts that a weak attraction between two substituted Nb atoms, a substituted Nb atom and a vacancy having strong attraction at the first nearest neighbour site and weak repulsive force at the second nearest neighbour site. The results of the present potential prediction are consistent with the DFT results.

Solute atoms can not only form at the substitution sites but also in interstitial positions, such as $\langle 100 \rangle$, $\langle 110 \rangle$ and $\langle 111 \rangle$ dumbbell, tetrahedral and octahedral positions. Most of the interstitial defects produced by irradiation damage will exist as the most stable interstitial structure, with different interstitial defects diffusing in different ways and corresponding to different migration energies. Therefore, the potential reasonably predicts the most stable interstitial structure is very important for subsequent micro-evolution. The most stable interstitial structure containing one Nb atom and two Nb atoms in BCC V predicted by the present potential is Nb-V $\langle 111 \rangle$ dumbbell and Nb-Nb $\langle 111 \rangle$ dumbbell, respectively, which is consistent with the DFT results. And the formation energies of interstitial structures are also close to the DFT results. The binding energy between a V-V $\langle 111 \rangle$ dumbbell and a substitutional Nb atom is −0.31 eV (forming a V-Nb $\langle 111 \rangle$ mixed dumbbell), which is slightly higher than the DFT calculation results of −0.49 eV. The binding energy between a mix V-Nb $\langle 111 \rangle$ dumbbell and a substitutional Nb atom is −0.32 eV (forming Nb-Nb $\langle 111 \rangle$ dumbbell), which is slightly higher than the DFT calculation result of −0.51 eV. However, both the present potential and the DFT results show that the binding energies between a substitutional solute Nb atom with a V-V $\langle 111 \rangle$ dumbbell or a mix V-Nb $\langle 111 \rangle$ dumbbell are negative, with repulsive forces. And both the present potential and

the DFT results show that the repulsion between a substituted solute Nb atoms and the V-V $\langle 111 \rangle$ dumbbell is weaker than that of the V-Nb $\langle 111 \rangle$ dumbbell.

Figure 4 shows some complex defect structures, and figure 4(a) shows the structure of two substituted atoms (substituted atoms B and C at the second nearest neighbours sites) and one vacancy (at the first nearest neighbour of the substituted atom) in bulk A. Figure 4(b) shows the structure of two substituted atoms (substituted atoms B and C at the third nearest neighbours sites) and one vacancy (at the first nearest neighbour of the substituted atom) in bulk A. Figure 4(c) shows the structure of three substituted atoms B, C and D in bulk A, where the two second nearest neighbour substitution site atoms (C and D) are located at the first nearest neighbour sites of substitution atom B. Figure 4(d) shows the structure between three substituted atoms (B, C and D) and one vacancy in bulk A, where the three substitution atoms (B, C and D) are located at the first nearest neighbour of the vacancy.

As shown in table 5, the defect properties of Nb and Ti together as solute atoms and the defect properties of Nb and Ta together as solute atoms in bulk V were calculated. The formation and binding energies of the two substituted solute atoms (Nb and Ti) at the first and second nearest neighbour sites are closed with the DFT results. And both the present potential and DFT calculations show that the binding energies of the two substituted solute atoms (Nb and Ti) in bulk V are positive and weakly attractive. The formation energies of the two substitutional atoms [(Nb-Ti) $_{2\text{nn}}$ and (Nb-Ti) $_{3\text{nn}}$] and one vacancy at their first nearest neighbour sites are 2.70 and 2.69 eV, which are slightly higher than the DFT calculation results (2.41 and 2.29 eV). And the corresponding binding energies are slightly lower than the DFT results (0.61 and 0.73 eV). However, both the present potential and DFT calculations show that the binding energies between the two substituted atoms and one vacancy are positive. The presence of a vacancy around the two substituted atoms increases the binding energy. The present potential results show that the most stable mixed Nb-Ti dumbbell in V is in the $\langle 110 \rangle$ direction, while the other two directions $\langle 100 \rangle$ and $\langle 111 \rangle$ are unstable, which is consistent with DFT results. The potential calculation of $\langle 110 \rangle$ dumbbell formation and binding energy are 4.60 and −0.39 eV, respectively, which are close to the DFT calculation results (4.29 and −0.41 eV).

The present potential predicts that the formation energies (0.44 and 0.36 eV) and binding energies (−0.01 and 0.07 eV) of the substituted Nb and Ta at the first and second nearest neighbour sites are close to the DFT calculation results (0.49, 0.45, 0.00 and 0.05 eV). Both the present potential and DFT calculations show that the binding energy of the two substitutional atoms (Nb and Ta) at the first nearest neighbour is close to 0, the binding energy at the second nearest neighbour is slightly greater than 0, and the force is very weak. The formation and binding energies between the two substitutional atoms [(Nb-Ta) $_{2\text{nn}}$ and (Nb-Ta) $_{3\text{nn}}$] and one vacancy at their first nearest neighbour site are close to the DFT results. The DFT calculations show that the most stable mixed Nb-Ta dumbbell in bulk V is in the $\langle 110 \rangle$ direction, while the $\langle 100 \rangle$ and $\langle 111 \rangle$ directions are unstable. Except for

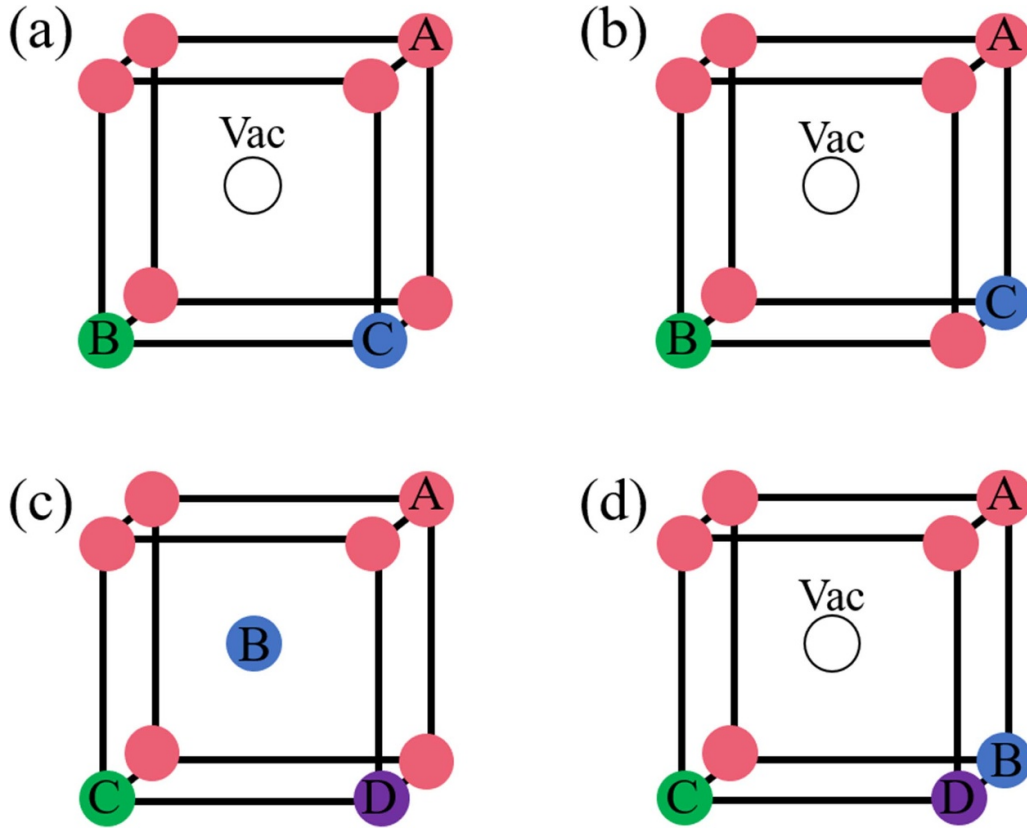


Figure 4. List complex defect atom configurations. (a) and (b) The configuration of two substitute atoms (B and C) and one vacancy in BCC bulk A, the corresponding formation energy be expressed as $E_{1nn}^f(\text{Vac} - (\text{B} - \text{C}) 2nn)$ and $E_{1nn}^f(\text{Vac} - (\text{B} - \text{C}) 3nn)$. (c) The configuration of three substitute atoms B, C and D in BCC bulk A, the corresponding formation energy be expressed as $E_{1nn}^f(\text{B} - (\text{C} - \text{D}) 2nn)$. (d) The configuration of three substitute atoms (B, C and D) and one vacancy in BCC bulk A, the corresponding formation energy be expressed as $E_{1nn}^f(\text{Vac} - (\text{D} - (\text{B} - \text{C}) 3nn) 2nn)$.

Table 5. Summary of the properties of solute atoms Nb and X (Ti or Ta) as the point defects in BCC bulk V calculated by the present potential in comparison with our DFT calculations. Including the formation energy and binding energy of two substitution atoms Nb and X located at the first and second neighbour sites, the formation energy and binding energy between two substitution atoms (Nb and X) and a vacancy, and the formation and binding energy of mixed dumbbell. The corresponding specific defect configurations are shown in figure 4.

| Property | FS present | DFT | Property | FS present | DFT |
|---|------------|----------|---|------------|----------|
| $E_{1nn}^f(\text{Nb} - \text{Ti})$ | 0.52 | 0.53 | $E_{1nn}^f(\text{Nb} - \text{Ta})$ | 0.44 | 0.49 |
| $E_{2nn}^f(\text{Nb} - \text{Ti})$ | 0.47 | 0.49 | $E_{2nn}^f(\text{Nb} - \text{Ta})$ | 0.36 | 0.45 |
| $E_{1nn}^b(\text{Nb} - \text{Ti})$ | 0.001 | 0.01 | $E_{1nn}^b(\text{Nb} - \text{Ta})$ | -0.01 | 0.00 |
| $E_{2nn}^b(\text{Nb} - \text{Ti})$ | 0.06 | 0.04 | $E_{2nn}^b(\text{Nb} - \text{Ta})$ | 0.07 | 0.05 |
| $E_{1nn}^f(\text{Vac} - (\text{Nb} - \text{Ti}) 2nn)$ | 2.70 | 2.41 | $E_{1nn}^f(\text{Vac} - (\text{Nb} - \text{Ta}) 2nn)$ | 2.52 | 2.46 |
| $E_{1nn}^f(\text{Vac} - (\text{Nb} - \text{Ti}) 3nn)$ | 2.69 | 2.29 | $E_{1nn}^f(\text{Vac} - (\text{Nb} - \text{Ta}) 3nn)$ | 2.37 | 2.33 |
| $E_{1nn}^b(\text{Vac} - (\text{Nb} - \text{Ti}) 2nn)$ | 0.38 | 0.61 | $E_{1nn}^b(\text{Vac} - (\text{Nb} - \text{Ta}) 2nn)$ | 0.47 | 0.52 |
| $E_{1nn}^b(\text{Vac} - (\text{Nb} - \text{Ti}) 3nn)$ | 0.39 | 0.73 | $E_{1nn}^b(\text{Vac} - (\text{Nb} - \text{Ta}) 3nn)$ | 0.62 | 0.66 |
| $E_{110}^f(\text{Nb} - \text{Ti})$ | 4.60 | 4.29 | $E_{110}^f(\text{Nb} - \text{Ta})$ | Unstable | 5.08 |
| $dE_{110-111}^f(\text{Nb} - \text{Ti})$ | Unstable | Unstable | $dE_{110-111}^f(\text{Nb} - \text{Ta})$ | unstable | Unstable |
| $dE_{110-111}^f(\text{Nb} - \text{Ti})$ | Unstable | Unstable | $dE_{110-111}^f(\text{Nb} - \text{Ta})$ | Unstable | Unstable |
| $E_{110}^b(\text{Nb} - \text{Ti})$ | -0.39 | -0.41 | $E_{110}^b(\text{Nb} - \text{Ta})$ | Unstable | -1.24 |

the $\langle 100 \rangle$ Nb-Ta dumbbell and $\langle 111 \rangle$ Nb-Ta dumbbell, the present potential calculations found that the $\langle 110 \rangle$ Nb-Ta dumbbell is also unstable. This may be because the binding energy of the Nb-Ta mixed dumbbell calculated by DFT is -1.24 eV, indicating that the mixed dumbbell formed by Nb

and Ta has a strong repulsive force, hence the instability of the Nb-Ta mixed dumbbell.

Table 6 shows a summary of the key characteristics of solute atoms Nb, Ti and Ta together as point defects in BCC bulk V and compared with our DFT calculations. The

Table 6. Summary of the key properties of three solute atoms Nb, Ti and Ta as the point defects in BCC bulk V calculated by the present potential in comparison with our DFT calculations. Including the formation energy and binding energy of three substitution atoms Nb, Ti and Ta, the formation energy and binding energy between three substitution atoms (Nb, Ti and Ta) and a vacancy. The corresponding specific defect configurations are shown in figure 4.

| Property | FS present | DFT |
|--|------------|------|
| E_{1nn}^f (Nb – (Ti – Ta) 2nn) | 0.71 | 0.73 |
| E_{1nn}^f (Ta – (Ti – Nb) 2nn) | 0.70 | 0.76 |
| E_{1nn}^f (Ti – (Ta – Nb) 2nn) | 0.65 | 0.75 |
| E_{1nn}^b (Nb – (Ti – Ta) 2nn) | 0.00071 | 0.04 |
| E_{1nn}^b (Ta – (Ti – Nb) 2nn) | 0.01 | 0.01 |
| E_{1nn}^b (Ti – (Ta – Nb) 2nn) | 0.06 | 0.02 |
| E_{1nn}^f (Vac – (Nb – (Ti – Ta) 3nn) 2nn) | 2.66 | 2.44 |
| E_{1nn}^f (Vac – (Ta – (Nb – Ti) 3nn) 2nn) | 2.68 | 2.44 |
| E_{1nn}^f (Vac – (Ti – (Nb – Ta) 3nn) 2nn) | 2.55 | 2.40 |
| E_{1nn}^b (Vac – (Nb – (Ti – Ta) 3nn) 2nn) | 0.61 | 0.82 |
| E_{1nn}^b (Vac – (Ta – (Nb – Ti) 3nn) 2nn) | 0.59 | 0.83 |
| E_{1nn}^b (Vac – (Ti – (Nb – Ta) 3nn) 2nn) | 0.71 | 0.86 |

corresponding specific defect configurations are shown in figure 4. The formation energies of the three substitution atoms Ta, Ti and Nb in bulk V calculated by the present potential are 0.71, 0.70 and 0.65 eV, which are close to the results of DFT calculations (0.73, 0.76 and 0.75 eV). And the binding energies of the three configurations are all positive and close to 0 (0.00, 0.01 and 0.06 eV), which are consistent with the DFT results (0.04, 0.01 and 0.02 eV), indicating that the interaction force of the three substitutional atoms is weakly attractive. The interaction between the three substitutional atoms Ti, Ta and Nb in V with one vacancy is also calculated by the present potential and compared with the DFT results. The formation energy between three substitutional atoms and one vacancy is about 2.6 eV [E_{1nn}^f (Vac – (B – (C – D) 3nn) 2nn)], which is close to the DFT result of 2.4 eV and the deviation is within 10%. The binding energies between the three substitution atoms and one vacancy predicted by the present potential are about 0.6 eV, which is close to the DFT result of 0.8 eV. The above results show that when there is a vacancy near the substitution atoms (Nb, Ti and Ta) in bulk V, the binding energy increases significantly, from weak attraction to a strong attraction force.

3.2.2. Mixing enthalpy for binary alloys. To verify the accuracy of the alloy potential, we calculated the mixing enthalpies of three disordered V-Nb, Ta-Nb and Ti-Nb alloys using the present potential and compared them with the corresponding DFT results [70, 71]. The mixing enthalpy of binary AB alloys is defined as follows:

$$\Delta H(A_{(1-x)}B_x) = H(A_{(1-x)}B_x) - (1-x)H(A) - xH(B) \quad (10)$$

Here x represents the concentration of B in alloy AB, $H(A_{(1-x)}B_x)$ is the enthalpy per atom of the solid solution formed, $H(A)$ and $H(B)$ are the enthalpies per atom of the

element in its ground state structure (bcc-Ta, V and Nb and hcp-Ti). The mixing enthalpy in this study was obtained in $10a \times 10a \times 10a$ boxes at zero temperature and zero pressure. Considering that the results of the DFT mixing enthalpy are not a specific structure, 2000 different conformations were calculated at each concentration using the present potential by the MD method to reduce the influence of random factors. Figure 5 shows the formation enthalpies of V-Nb alloys predicted by the present potential and compared with the DFT results [70]. The present potential predicted results and DFT results show that the formation enthalpy of V-Nb alloys with different proportions is always positive, and the mixing enthalpies are the largest when the alloy concentration reaches 1:1. The predicted values are within the range of DFT calculation results, which are consistent with DFT results. Figure 6 shows the formation enthalpies of Nb-Ta alloys predicted by the present potential and compared with the DFT results [70]. The mixing enthalpies of Nb-Ta alloy calculated by the present potential are negative, which is consistent with the DFT results. And the present potential predicts that the most stable mixing enthalpies of alloys with different ratios are close to the DFT results.

As shown in figure 7, we calculated the mixing enthalpies of BCC Nb-Ti alloy and HCP Ti-Nb alloy by the present potential and compared them with the DFT results [71]. Figure 7(a) shows the mixing enthalpy of BCC Nb-Ti alloy as a function of concentration. Although the mixed enthalpy results predicted by the present potential are slightly larger than the DFT results [71]. The present potential prediction results show that the mixing enthalpies of BCC Nb-Ti alloy gradually increase with increasing Ti concentration, which is consistent with the DFT trend. In addition, the mixed enthalpies of BCC Nb-Ti alloys predicted by present potential are all positive, which is also consistent with the DFT results [71]. Figure 7(b) shows the mixing enthalpy of the HCP Ti-Nb alloy as a function of Nb concentration. The mixing enthalpies of HCP Ti-Nb alloy predicted by the present potential increase gradually with the increase of Nb concentration, and the mixing enthalpies are all positive, which is consistent with the DFT results. And the value of mixing enthalpies predicted by present potential is close to the DFT results [71].

The results show that the mixed enthalpies of Ta-Nb alloy predicted by the potential are negative, while the mixed enthalpies of V-Nb and Ti-Nb alloy are positive, which is consistent with the DFT results [70, 71]. And a negative alloy mixing enthalpy means that the alloy is thermodynamically stable, while a positive alloy mixing means that it is thermodynamically unstable. Overall, the present potential reproduces the mixing enthalpy of the alloy, confirming the accuracy of the potential.

3.3. Displacement cascade simulation for V-Ti-Ta-Nb HEAs

To further verify the radiation nature of the alloy potential, we investigated the displacement cascades of quaternary V-Ti-Ta-Nb HEAs using the Large Atom/ Molecular Massively Parallel Simulator [72]. The entire simulation is performed in a box of $150a_0 \times 150a_0 \times 150a_0$ (a_0 is the lattice constant),

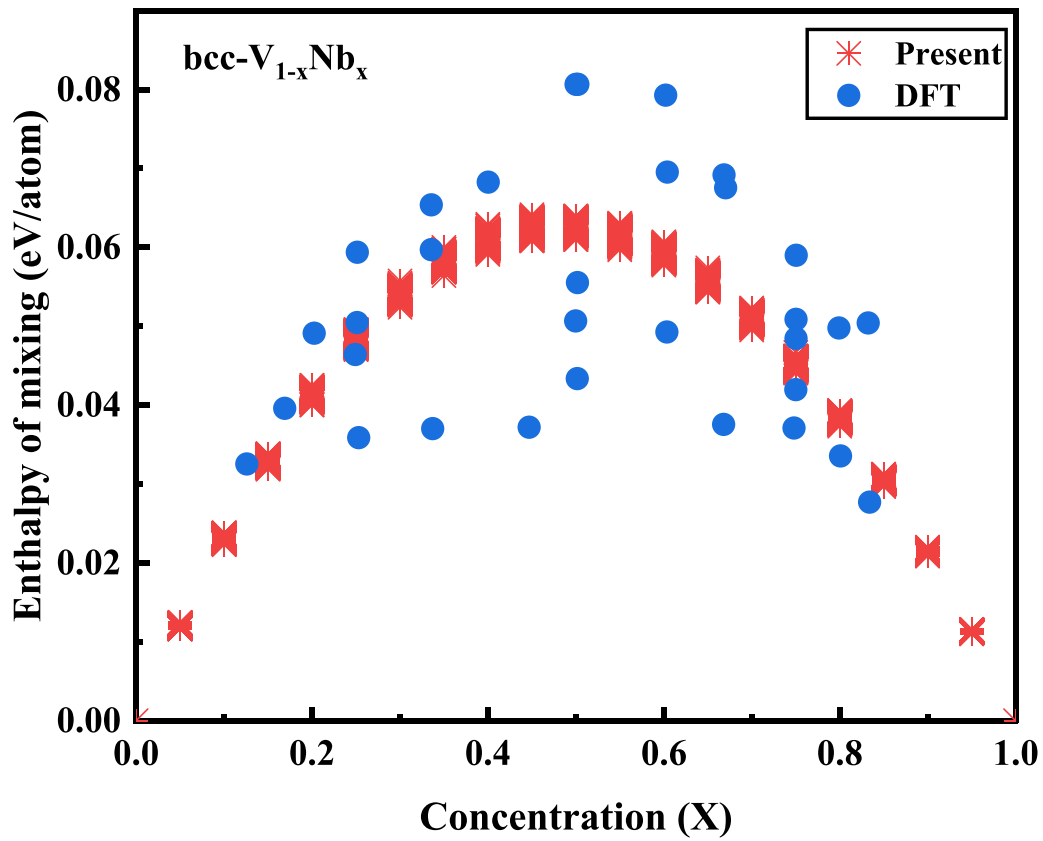


Figure 5. Compared mixing enthalpies of disordered BCC V-Nb alloys as a function of the Nb concentration predicted by the present potential (2000 different structures at the same concentration) and the DFT results [70].

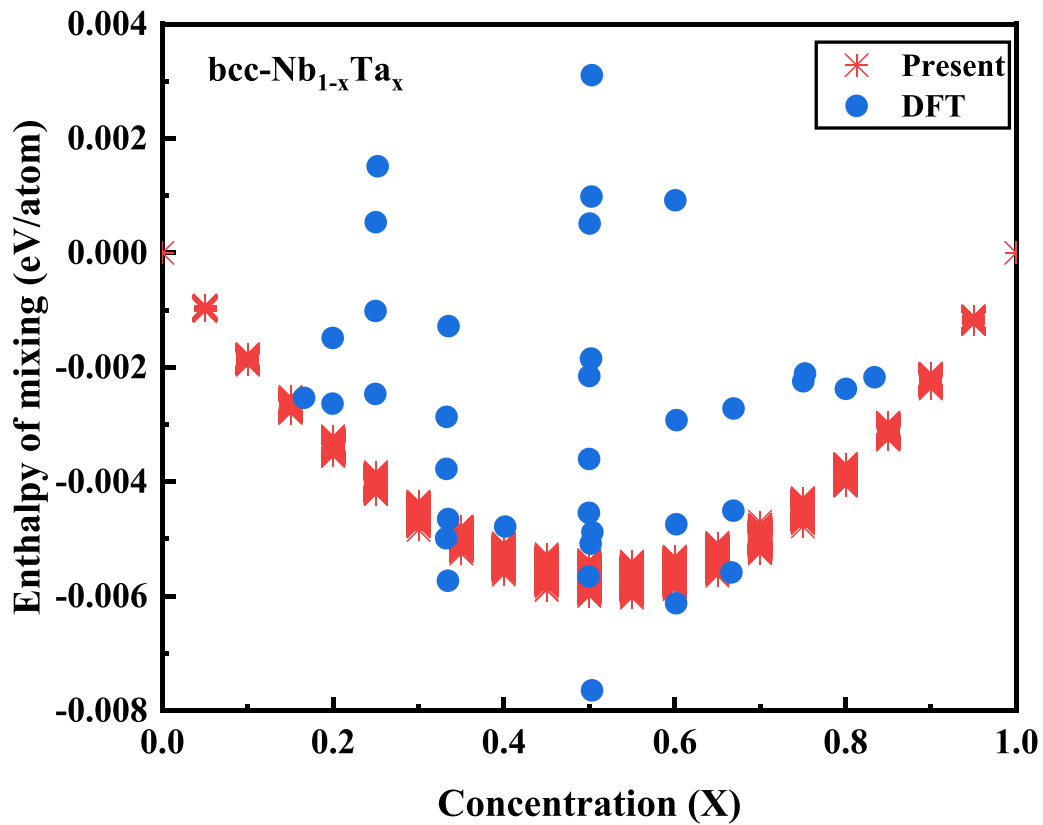


Figure 6. Compared mixing enthalpies of disordered BCC Ta-Nb alloys as a function of the Ta concentration predicted by the present potential (2000 different structures at the same concentration) and the DFT results [70].

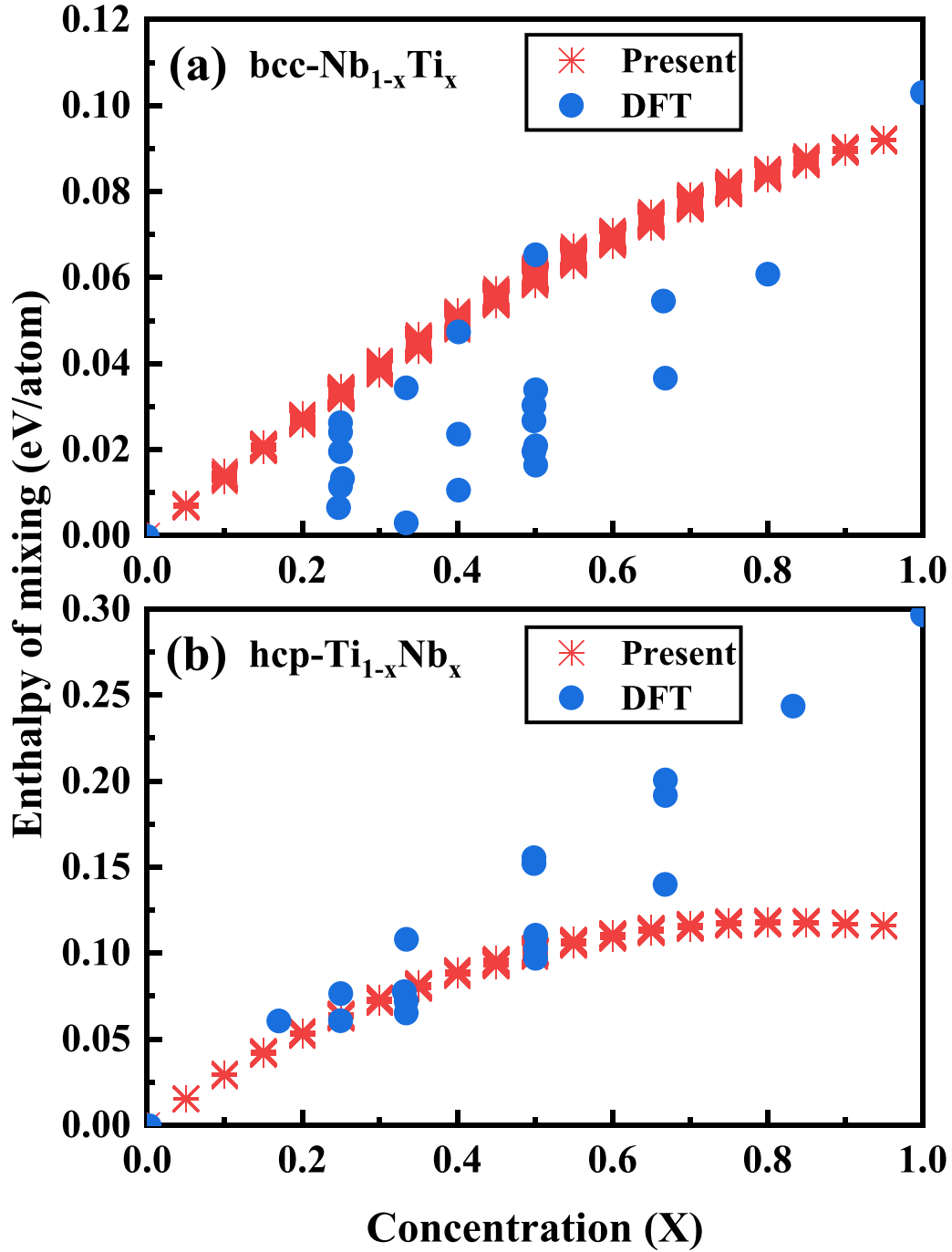


Figure 7. Compared mixing enthalpies of disordered BCC Nb-Ti and HCP Ti-Nb alloys predicted by the present potential (2000 different structures at the same concentration) and the DFT results [71].

and periodic boundary conditions are used in all three dimensions. The primary knock-on atom (PKA) is a randomly selected V atom with initial velocity in the high-exponential direction $\langle 135 \rangle$ to avoid channelling effects [73]. A variable time step (10^{-3} – 10^{-7} ps) was applied throughout the cascade, and the canonical (NVT) ensemble was applied to the outermost boundary of the box with a thickness of three lattice layers (six atomic layers), microcanonical (NVE) ensemble is applied to the inner atoms of the simulation box. More specific simulation methods can refer to previous work [74–76].

Figure 8 shows the collision cascade process with a PKA energy of 50 keV at 300 K. Figure 8(a) shows the evolution of the Frenkel pairs (FPs) number, figures 8(b)–(d) are initial collision stage, thermal spike and the remaining stage of primary damage, respectively. For clarity, only part of the simulation cell is shown. As shown in figure 8(a), according to previous studies [76–78], the cascade process can be divided into three stages. In the stage I, the number of FPs increases rapidly and then reaches the maximum value (thermal spike) (corresponding to figure 8(c)); in the stage II, a large number

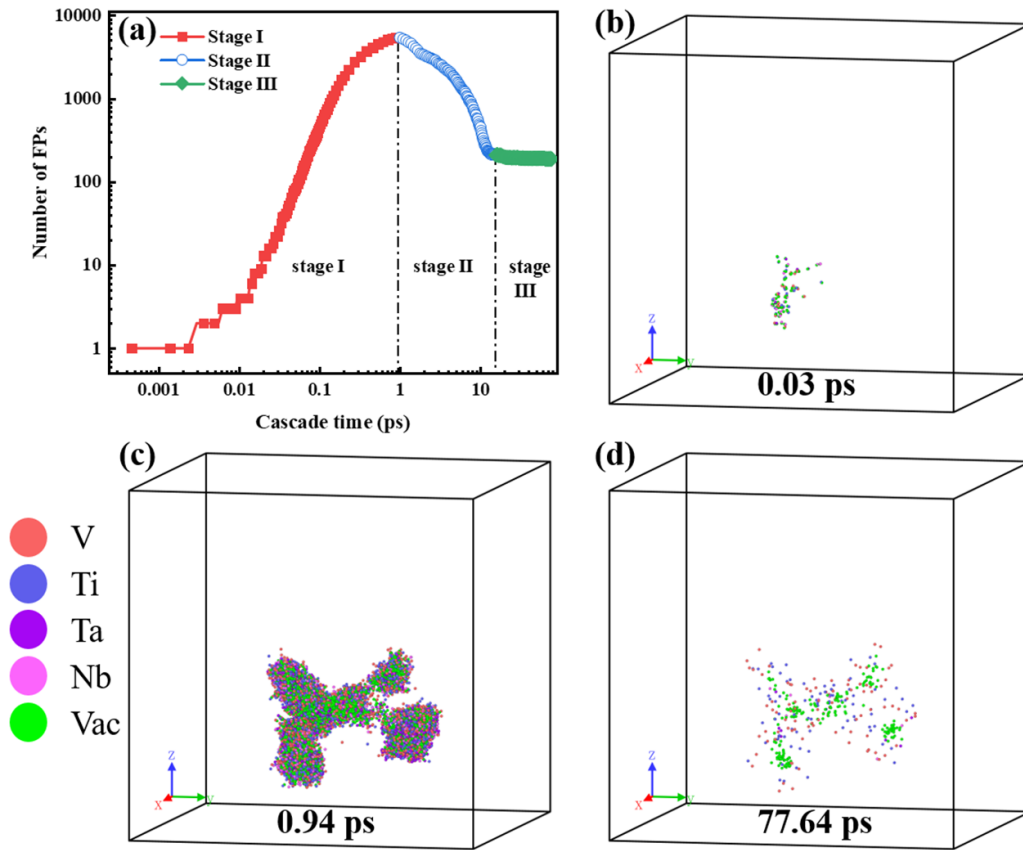


Figure 8. Snapshots of the cascade process. Displacement cascade of a primary knocked-on atom with the kinetic energy of 50 keV along the $\langle 135 \rangle$ direction. (a) Evolution of the number of Frenkel pairs (b) initial stage, (b) thermal spike and (f) final stage.

of interstitial and vacancy defects recombine, the number of FPs decreased rapidly, and a small number of FPs survive; in the stage III, the surviving FPs further evolve in the remaining stage of primary damage. Figure 8(c) shows the defect distribution at the time of the cascade thermal spike, the number of FPs reaches a maximum and several sub-cascades can be observed. Figure 8(d) shows the surviving defects of V-Ti-Ta-Nb alloy at the end of the collision cascade (77.64 ps). The entire process of defect evolution is provided in the supplementary material (figure 8-b-c-movie.mov). The whole process is consistent with the previous collision cascade results [75–79].

In order to study the irradiation damage of the V-Ti-Ta-Nb HEA, we simulated the displacement cascade of pure V and V-Ti-Ta-Nb HEA systems, and each system has 20 simulations. A total of 23 dislocation loops appear in the pure V system in the 20 simulations with PKA energies of 50 keV, while a total of 6 dislocation loops appear in the V-Ti-Ta-Nb HEA. The number of dislocation loops in the V-Ti-Ta-Nb HEA is much lower than in the pure V system under the same conditions. This is similar to previous studies of HEAs, where lattice distortion-related properties inhibit the evolution of defects, resulting in smaller defect sizes and fewer dislocation loops [35, 36, 80]. In addition, the equilibrium lattice constant of 3.24 Å at 0 K for the V-Ti-Ta-Nb HEA obtained in the simulation is equal to the DFT result [37]. Thus, the present potential can describe the collision cascade process of V-Ti-Ta-Nb HEAs.

The more detailed radiation damage simulation of V-Ti-Ta-Nb HEA will be systematically investigated in the next work.

4. Conclusions

In this work, we developed the FS type V-Ti-Ta-Nb quaternary interatomic potential for the first time by adding Nb as a new element based on the previously developed V-Ti-Ta ternary potential. In addition, the properties of a large number of point defects in V-based alloys with Ta, Ti and Nb as solute atoms were calculated by the first-principles method. The fitted properties of the pure Nb potential include lattice constants, cohesive energy, elastic constant, bulk modulus, structural energy difference, vacancy formation energy, vacancy migration energy and interstitial formation energy, and these quantities agree well with DFT or experiments. In addition to the fitted properties, the potential also exactly predicted the stacking fault energy, surface energy, melting point and relative stability of the $\langle 100 \rangle$ and $1/2\langle 111 \rangle$ interstitial dislocation loops. The most excellent property of pure Nb potential is that the most stable interstitial defect calculated by it is consistent with the DFT results, the most stable interstitial form is crucial for reproducing the displacement cascade process. In addition, the properties of point defects in V-based alloys with Ta, Ti and Nb as solute atoms calculated by the present potential are consistent with the DFT results, including the

solute atoms at the substitution position, the solute atoms at the substitution position near a vacancy and the solute atom as the interstitial. The predicted mixing enthalpies of the three binary alloys are acceptable compared to the DFT results. The developed potential can be used to determine the defect-properties of V-Ti-Ta-Nb alloys, and can be employed to study defect production, defect interaction with microstructural features and microstructural evolution in V-Ti-Ta-Nb alloys under irradiation.

Data availability statement

The data that support the findings of this study are available upon reasonable request from the authors.

Acknowledgments

This work was financially supported by the CNNC Science Fund for Talented Young Scholars (FY202307000120) and the Continuous Basic Scientific Research Project (WDJC-2019-10).

ORCID iDs

Xichuan Liao  <https://orcid.org/0000-0001-6172-6997>
Huiqiu Deng  <https://orcid.org/0000-0001-8986-104X>

References

- [1] Yeh J W, Chen S K, Lin S J, Gan J-Y, Chin T S, Shun T, Tsau C H and Chang S Y 2004 *Adv. Eng. Mater.* **6** 299
- [2] Cantor B, Chang I, Knight P and Vincent A J B 2004 *Mater. Sci. Eng. A* **375–377** 213
- [3] Shi Y, Yang B and Liaw P 2017 *Metals* **7** 43
- [4] He Q F, Ding Z Y, Ye Y F and Yang Y 2017 *JOM* **69** 2092
- [5] Ye Y F, Wang Q, Lu J, Liu C T and Yang Y 2016 *Mater. Today* **19** 349
- [6] Tsai M H and Yeh J W 2014 *Mater. Sci. Lett.* **2** 107
- [7] Gludovatz B, Hohenwarther A, Catoor D, Chang E H, George E P and Ritchie R O 2014 *Science* **345** 1153
- [8] Aravindh S A, Kistanov A A, Alatalo M, Kömi J, Huttula M and Cao W 2021 *J. Phys.: Condens. Matter* **33** 135703
- [9] Cao P, Ni X, Tian F, Varga L K and Vitos L 2015 *J. Phys.: Condens. Matter* **27** 075401
- [10] Senkov O N, Wilks G B, Miracle D B, Chuang C P and Liaw P K 2010 *Intermetallics* **18** 1758
- [11] Gao M C, Carney C S, Doğan Ö N, Jablonksi P D, Hawk J A and Alman D E 2015 *JOM* **67** 2653
- [12] Wu Z, Bei H, Otto F, Pharr G M and George E P 2014 *Intermetallics* **46** 131
- [13] Takeuchi A, Amiya K, Wada T, Yubuta K and Zhang W 2014 *JOM* **66** 1984
- [14] Gao M C, Zhang B, Guo S M, Qiao J W and Hawk J A 2016 *Metall. Mater. Trans. A* **47** 3322
- [15] Zhao Y J, Qiao J W, Ma S G, Gao M C, Yang H J, Chen M W and Zhang Y 2016 *Mater. Des.* **96** 10
- [16] Lu C et al 2017 *Acta Mater.* **127** 98
- [17] Gludovatz B, Hohenwarther A, Thurston K V, Bei H, Wu Z, George E P and Ritchie R O 2016 *Nat. Commun.* **7** 10602
- [18] He J Y, Liu W H, Wang H, Wu Y, Liu X J, Nieh T G and Lu Z P 2014 *Acta Mater.* **62** 105
- [19] Lu C et al 2016 *Nat. Commun.* **7** 13564
- [20] Varvenne C, Luque A and Curtin W A 2016 *Acta Mater.* **118** 164
- [21] Rao Z, Wang X, Wang Q, Liu T, Chen X, Wang L and Hui X 2017 *Adv. Eng. Mater.* **19** 1600726
- [22] Chen Y Y, Duval T, Hung U D, Yeh J W and Shih H C 2005 *Corros. Sci.* **47** 2257
- [23] Zhang Y, Osetsy Y N and Weber W J 2022 *Chem. Rev.* **122** 789
- [24] Zhang Y, Zhao S, Weber W J, Nordlund K, Granberg F and Djurabekova F 2017 *Curr. Opin. Solid State Mater. Sci.* **21** 221
- [25] Zhang Y et al 2016 *J. Mater. Res.* **31** 2363
- [26] Granberg F, Nordlund K, Ullah M W, Jin K, Lu C, Bei H, Wang L M, Djurabekova F, Weber W J and Zhang Y 2016 *Phys. Rev. Lett.* **116** 135504
- [27] Yeh J W, Chen S K, Gan J Y, Lin S J, Chin T S, Shun T T, Tsau C H and Chang S Y 2004 *Metall. Mater. Trans. A* **35a** 2533
- [28] Zhang Y, Zuo T T, Tang Z, Gao M C, Dahmen K A, Liaw P K and Lu Z P 2014 *Prog. Mater. Sci.* **61** 1
- [29] Tong C J, Chen M R, Yeh J W, Lin S J, Chen S K, Shun T T and Chang S Y 2005 *Metall. Mater. Trans. A* **36** 1263
- [30] Zhang Y, Yang X and Liaw P K 2012 *JOM* **64** 830
- [31] Senkov O N, Wilks G B, Scott J M and Miracle D B 2011 *Intermetallics* **19** 698
- [32] El-Atwani O et al 2019 *Sci. Adv.* **5** eaav2002
- [33] Barron P J, Carruthers A W, Fellowes J W, Jones N G, Dawson H and Pickering E J 2020 *Scr. Mater.* **176** 12
- [34] Sun Z and Cui H 2018 *J. Mater. Eng. Perform.* **27** 3394
- [35] Sadeghilaridjani M, Ayyagari A, Muskeri S, Hasannaeimi V, Salloom R, Chen W-Y and Mukherjee S 2020 *J. Nucl. Mater.* **529** 151955
- [36] Kareer A, Waite J C, Li B, Couet A, Armstrong D E J and Wilkinson A J 2019 *J. Nucl. Mater.* **526** 151744
- [37] Lee C et al 2018 *Acta Mater.* **160** 158
- [38] Yao H W, Qiao J W, Hawk J A, Zhou H F, Chen M W and Gao M C 2017 *J. Alloys Compd.* **696** 1139
- [39] Yao H W, Qiao J W, Gao M C, Hawk J A, Ma S G, Zhou H F and Zhang Y 2016 *Mater. Sci. Eng. A* **674** 203
- [40] Qiu R, Chen Y, Liao X, He X, Yang W, Hu W and Deng H 2021 *J. Nucl. Mater.* **557** 153231
- [41] Fellingner M R, Park H and Wilkins J W 2010 *Phys. Rev. B* **81** 144119
- [42] Cheng C, Ma Y, Bao Q, Wang X, Sun J, Zhou G, Wang H, Liu Y and Xu D 2020 *Comput. Mater. Sci.* **173** 109432
- [43] Yang C and Qi L 2019 *Comput. Mater. Sci.* **161** 351
- [44] Roberge R 1975 *J. Less-Common Met.* **40** 161
- [45] Kittel C 1996 *Introduction to Solid State Physics, 7th ed* (New York: Wiley)
- [46] Simmons G and Wang H 1971 *Single Crystal Elastic Constants and Calculated Aggregate Properties: A Handbook* (Cambridge, MA: MIT Press)
- [47] Ullmaier H 1991 *Atomic Defects in Metals / Atomare Fehlstellen in Metallen* (Berlin: Springer)
- [48] Cerdeira M A, Palacios S L, González C, Fernández-Pello D and Iglesias R 2016 *J. Nucl. Mater.* **478** 185
- [49] Chen Y, Fang J, Liu L, Hu W, Gao N, Gao F and Deng H 2019 *Comput. Mater. Sci.* **163** 91
- [50] Chen Y, Liao X, Gao N, Hu W, Gao F and Deng H 2020 *J. Nucl. Mater.* **531** 152020
- [51] Chen Y, Fang J, Liao X, Gao N, Hu W, Zhou H-B and Deng H 2021 *J. Nucl. Mater.* **549** 152913
- [52] Chen Y, Li Y-H, Gao N, Zhou H-B, Hu W, Lu G-H, Gao F and Deng H 2018 *J. Nucl. Mater.* **502** 141
- [53] Bonny G and Pasianot R C 2010 *Phil. Mag. Lett.* **90** 559
- [54] Johnson R A and Oh D J 1989 *J. Mater. Res.* **4** 1195

- [55] Ziegler J F, Biersack J P and Littmark U 1985 *The Stopping and Range of Ions in Matter* (New York: Pergamon)
- [56] Kirkpatrick S, Gelatt C D Jr and Vecchi M P 1983 *Science* **220** 671
- [57] Møller M F 1993 *Neural Netw.* **6** 525
- [58] Rose J H, Smith J R, Guinea F and Ferrante J 1984 *Phys. Rev. B* **29** 2963
- [59] Gao F, Deng H, Heinisch H L and Kurtz R J 2011 *J. Nucl. Mater.* **418** 115
- [60] Bonny G, Terentyev D, Bakaev A, Grigorev P and Van Neck D 2014 *Modelling Simul. Mater. Sci. Eng.* **22** 053001
- [61] Liao X et al 2020 *J. Nucl. Mater.* **541** 152421
- [62] Kresse G and Hafner J 1993 *Phys. Rev. B* **47** 558
- [63] Kresse G and Furthmüller J 1996 *Phys. Rev. B* **54** 11169
- [64] Blochl P E 1994 *Phys. Rev. B* **50** 17953
- [65] Shang S-L, Zhou B-C, Wang W Y, Ross A J, Liu X L, Hu Y-J, Fang H-Z, Wang Y and Liu Z-K 2016 *Acta Mater.* **109** 128
- [66] Yao Z, Jenkins M L, Hernández-Mayoral M and Kirk M A 2010 *Phil. Mag.* **90** 4623
- [67] Yi X O, Jenkins M L, Hattar K, Edmondson P D and Roberts S G 2015 *Acta Mater.* **92** 163
- [68] Horton L L and Farrell K 1984 *J. Nucl. Mater.* **122** 687
- [69] Alexander R, Marinica M C, Provile L, Willaime F, Arakawa K, Gilbert M R and Dudarev S L 2016 *Phys. Rev. B* **94** 024103
- [70] Ravi C, Panigrahi B K, Valsakumar M C and van de Walle A 2012 *Phys. Rev. B* **85** 054202
- [71] Chinnappan R, Panigrahi B K and van de Walle A 2016 *Calphad* **54** 125
- [72] Plimpton S 1995 *J. Comput. Phys.* **117** 1
- [73] Stoller R E 2000 *J. Nucl. Mater.* **276** 22
- [74] Fu J, Chen Y, Fang J, Gao N, Hu W, Jiang C, Zhou H-B, Lu G-H, Gao F and Deng H 2019 *J. Nucl. Mater.* **524** 9
- [75] Qiu R, Chen Y, Liu L, Liu Z, Gao N, Hu W and Deng H 2021 *J. Nucl. Mater.* **556** 153162
- [76] Lin Y, Yang T, Lang L, Shan C, Deng H, Hu W and Gao F 2020 *Acta Mater.* **196** 133
- [77] Nordlund K and Djurabekova F 2014 *J. Comput. Electron.* **13** 122
- [78] Nordlund K et al 2018 *J. Nucl. Mater.* **512** 450
- [79] Peng Q, Meng F, Yang Y, Lu C, Deng H, Wang L, De S and Gao F 2018 *Nat. Commun.* **9** 4880
- [80] Parkin C, Moorehead M, Elbakhshwan M, Hu J, Chen W-Y, Li M, He L, Sridharan K and Couet A 2020 *Acta Mater.* **198** 85